www.sciencemag.org/cgi/content/full/318/5850/623/DC1

Supporting Online Material for

Upper Mantle Discontinuity Topography from Thermal and Chemical Heterogeneity

Nicholas Schmerr* and Edward J. Garnero

*To whom correspondence should be addressed. E-mail: nschmer@asu.edu

Published 26 October 2007, *Science* **318**, 623 (2007)
DOI: 10.1126/science.1145962

This PDF file includes:

Materials and Methdos
Figs. S1 to S18
References

Supplemental Online Materials for:

Upper Mantle Discontinuity Topography from Thermal and Chemical Heterogeneity

Nicholas Schmerr[1]
Edward J. Garnero[1]

[1]Arizona State University, School of Earth and Space Exploration, Box 871404, Tempe, AZ 85287-1404

This PDF file includes:

Materials and Methods
Figs. S1 to S18
References

Details on the Method

Data for our study were downloaded from the Incorporated Research Institutions for Seismology (*S1*) and the Canadian National Seismic Network websites (*S2*). EarthScope's USArray data (*S3*) was extremely beneficial, providing hundreds of high-quality sensors in the western United States and bolstering coverage from existing global networks. We selected earthquakes for our study with source depths ≤ 75 km to avoid interference with depth phase energy (i.e., surface reflected waves), moment magnitudes ≥ 5.8 to insure sufficient energy amplitudes, epicentral distances between 100-165º, and SS surface bouncepoints within our study region (Fig. 1C). Data were band pass filtered between 10-75 seconds to remove long-period energy and high-frequency noise. Only data with high SS signal-to-noise ratios were retained; additional data selection criterion and processing analyses are given in detail in (12). The South American region of the globe is poorly sampled in past studies, a fact illustrated by poor agreement between previous topography models (7).

In stacking, we canvas our study area with 362 overlapping bins of 1000-km radius, approximately equally spaced 500-km apart. SS bouncepoint locations falling within each bin are non-uniform due to uneven earthquake and station geometry; hence each bin location is adjusted and centered on the average location of bouncepoints within that bin. We experimented with a variety of stacking geometries, including larger versus smaller spacing between bins, as well as tests involving randomly distributed bins with uneven spacing; we found that the resulting topography did not change meaningfully for various bin spacings, and evidence for multiple discontinuities noted in some regions remained intact. We experimented with a variety of bin sizes in an effort to minimize smoothing from overly large bins, but to have bins large enough to provide enough data for precursor amplitudes to fall above the 95% confidence interval. In general, bins with 1000-km radius produced the most stable tradeoff between these two values, and have the added benefit of roughly approximating the size of the SS Fresnel zone at 10 seconds dominant period.

As in (12), we separately stack data for underside reflections off either the 410-km or the 660-km phase boundary, S410S and S660S, respectively, utilizing their expected arrival time information versus epicentral distance (i.e., their moveout). SS precursor travel times are converted to discontinuity depth by introducing theoretical reflector depths in the PREM model (*S4*) and then interpolating between layers to match measured precursor arrival times. Crustal and surface topography are accounted for by using CRUST2.0 (*S5*) and ETOPO2.0 (*S6*), respectively. All corrections are computed relative to a dry (no ocean) reference PREM value. The mantle heterogeneity correction is calculated by 1-D ray-tracing through a suite of tomography models for the path of the SS and precursor phases. We investigated the dependency of retrieved discontinuity structure on the choice of tomography correction model, and found only small (insignificant) solution perturbations (Fig. S3).

Histograms of mantle transition zone (MTZ) thickness estimates (from the bootstrap resampling, as discussed in the main text) are presented for regions falling within 500 km of subduction zones, mantle hotspots, and mid-ocean ridges (Fig. S4). The mean MTZ thickness perturbation about the global value of 242 km beneath subduction zones and hotspots is 11 km thicker and 8 km thinner, respectively, for 10 second energy histograms. While these MTZ thickness deviations are consistent with a thermal origin to the 410-km and 660-km topography, there is significant complexity to the bootstrap-derived MTZ thickness histograms in the 10 sec data; for example, the MTZ beneath subduction zones has peaks at +7 and +20 km, and the MTZ beneath hotspots has peaks at –5, –12, and –23 km. This is not unexpected, since shorter period energy is sensitive to smaller scale structural features, and evidence for multiple discontinuities exists (Fig. 2).

We investigated the possible contribution of biases due to uneven earthquake/station azimuths for our data set, event depth, as well as corrections for mantle structure on our retrieved topography. We tested this using the bootstrap-resampling algorithm; for each random resample we computed the mode of the event azimuth (the average azimuth is less meaningful due to the distribution of event-station corridors predominantly being roughly bimodal), the average event depth, and the average tomographic and crustal thickness/topography correction for each resample. A bias toward one or two particular azimuths could conceivably introduce travel time anomalies from SS paths predominantly sampling fundamentally different upper mantle structures, such as slab parallel versus slab perpendicular ray paths. Bins exhibiting multiple precursors had azimuthal distributions very similar to bins with only a single precursory arrival, so we discount azimuthally dependent travel times as a source of this heterogeneity.

Similarly, a bias towards deep events for bouncepoints in a particular bin may lead to constructive interference of the depth phase sS410S and/or sS660S that would be mistaken for another reflector close to the S410S or S660S arrivals. In nearly all bins exhibiting multiple discontinuities, the bootstrapped event depth distributions were similar to those with only one reflector, making it unlikely the secondary arrivals are depth phase energy. The corrections for crustal structure and tomography were also distributed evenly within any given bin and showed a spread of no more than ±1-2 seconds, with no pronounced difference in this distribution between bins with multiple or singular arrivals. Only bins with an extremely small numbers of records (NR < 25) exhibited any bias towards particular event depths, corrections, or azimuths, though in these bins multiple reflectors were generally well below the 95% confidence interval from the bootstrap resampling, and do not affect our conclusions.

The largest excursion in the absolute depths of the discontinuities from the regional average occurs beneath the South American continent and mid-ocean ridges in our study region (Fig. S3). This roughly correlates with the location of the strongest shear wave anomalies of the upper mantle in the tomography models we use to correct for discontinuity depths (see Figs. S5-S15). Past studies [e.g., (5)] have cautioned over-interpretation of absolute discontinuity depth, as corrections from tomography may overestimate or under account for heterogeneity encountered by the SS phase in the upper mantle. The tomography models we use are relatively smooth and hence may also underestimate structure in regions of small-scale heterogeneity, especially near subduction (*S7*). Correction values for SS-S400S and SS-S660S travel times across our region have an absolute variation of –5 to +10 seconds, which can map to approximately –15 to +30 km of relief. Note that this correction is for the difference along the entire SS and precursor ray path, not just the upper mantle. Averaging over a large number of different ray paths finds that the correction within each bin is relatively small (2-3 seconds).

Given that this may map to absolute discontinuity depths, we calculate the shear wave velocity anomaly needed to remove the unexpectedly deep 10-15 km deep 410-km discontinuity in the down-dip direction of subduction beneath the north-central portion of South America. If this structure were induced by an erroneous correction for tomography, it would require that we either over-correct for the upper mantle structure encountered by the SS phase or under-correct for transition zone heterogeneity encountered by the S410S precursor underneath the continent (or a combination of both). In the former case, we compute that the shear wave velocity anomaly in the tomography models would need to be reduced by approximately 1.0-1.5% over the entire 410 km of the upper mantle to remove 10-15 km of topography on the 410- and 660-km discontinuities beneath the continent. In the latter, the velocities in the transition zone between the 660-km and the 410-km boundaries would be required to be approximately 3.0-3.5% higher than that in the models to correct for the excess topography on the discontinuities beneath the continent. In both scenarios, the mantle transition zone would still remain thickened. Reducing the velocity above the 410-km over the whole region is problematic – tomography, while inferring velocity depressions in some upper mantle regions, displays high velocities, consistent with the presence of a South American craton in the upper couple hundred kilometers, and cooler temperatures associated with the past and present subduction. Raising shear velocity by several percent in the transition zone alone is equally problematic, since we expect velocities raised above the transition zone as well, presumably due to lower temperature, which would counter this effect (since velocities above 410-km need to be lowered to offset our observed topography).

In addition, crustal structure can contribute a bias in the absolute depths of the discontinuities. The complex crustal structure beneath continents complicates the SS waveform and can lead to an offset of the peak arriving energy by 1-2 seconds (*S8*), though this effect is minimal for SS bouncepoints located beneath oceanic crust. This bias could introduce an unexpected 3-6 km of relief onto the discontinuities; however, we image topography beneath the continent of 10-15 km on the 410-km boundary, and 15-25 km of relief on the 660-km discontinuity, well in excess of this value. Additionally, this bias is predominantly present in longer period data, and reduced by the use of broadband seismograms and careful selection of clear SS arrivals.

We also investigate the shear wave velocity perturbations introduced by incorrectly mapping mantle velocities for slightly deeper or shallower discontinuities, for example, deepening the 410-km phase boundary results in lower velocities displacing higher velocities down to the deepened velocity discontinuity. However, we found this effect to be relatively small (< 0.5 seconds of delay for a 410-km discontinuity deepened by 20 km). Therefore, we conclude that the depths we image on the 410- and 660-km discontinuities are a result of topography and not systematic biases in our corrections for mantle heterogeneity.

Supplemental Figures and Captions:

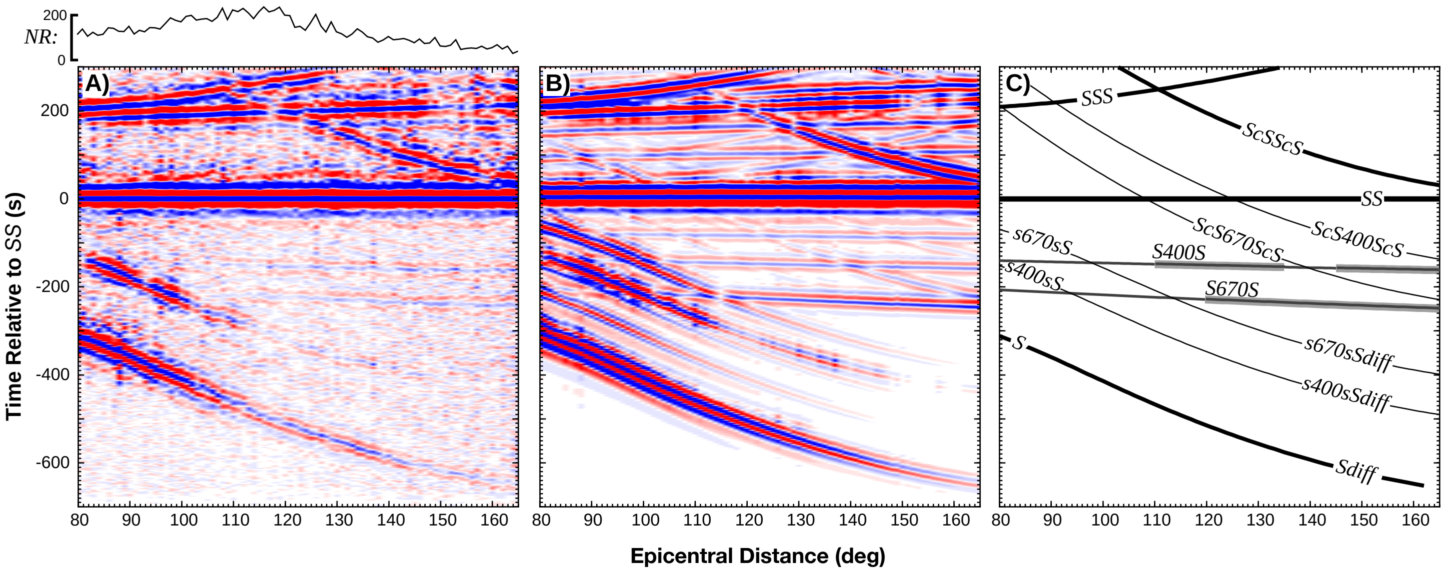

Fig. S1. Epicentral distance stacks for both (**A**) data and (**B**) reflectivity synthetic seismograms (*S9*) computed for the PREM (*S4*) 1-D reference Earth model, illustrating the dominant seismic arrivals preceding and following the SS wave. Positive and negative amplitudes are plotted as blue and red, respectively, with the maximum amplitude of SS normalized to one. (**A**) Stacked amplitudes of the data binned in 1-degree increments and aligned on SS. The data are filtered between 10 and 75 seconds to reduce high and low frequency noise content. The number of records in each stack is given above the stacked amplitudes. Note that there is a lack of evidence for a coherent arrival between S400S and S670S at 520-km depth in our study region, that is, S520S. A synthetic seismogram is computed for each record in the data stack, at the appropriate epicentral distance and event depth, then stacked in the same manner as the data. These are shown in panel (**B**). The PREM model has a first order discontinuity at 220-km depth, which appears as the coherent arrival in the synthetic stack between SS and S400S.

(**C**) PREM predicted travel times for selected phases in the precursor wave field. All phases in this figure are labeled according to their PREM discontinuity depths, 400-km and 670-km. Several phases pass through and interfere with the precursors; these epicentral distance windows are excluded in the geographic stacking of data to prevent contamination and blurring of the discontinuity arrivals. We highlight in light gray the distances that are acceptably free of this interference (also see Fig. S2 and (12)).

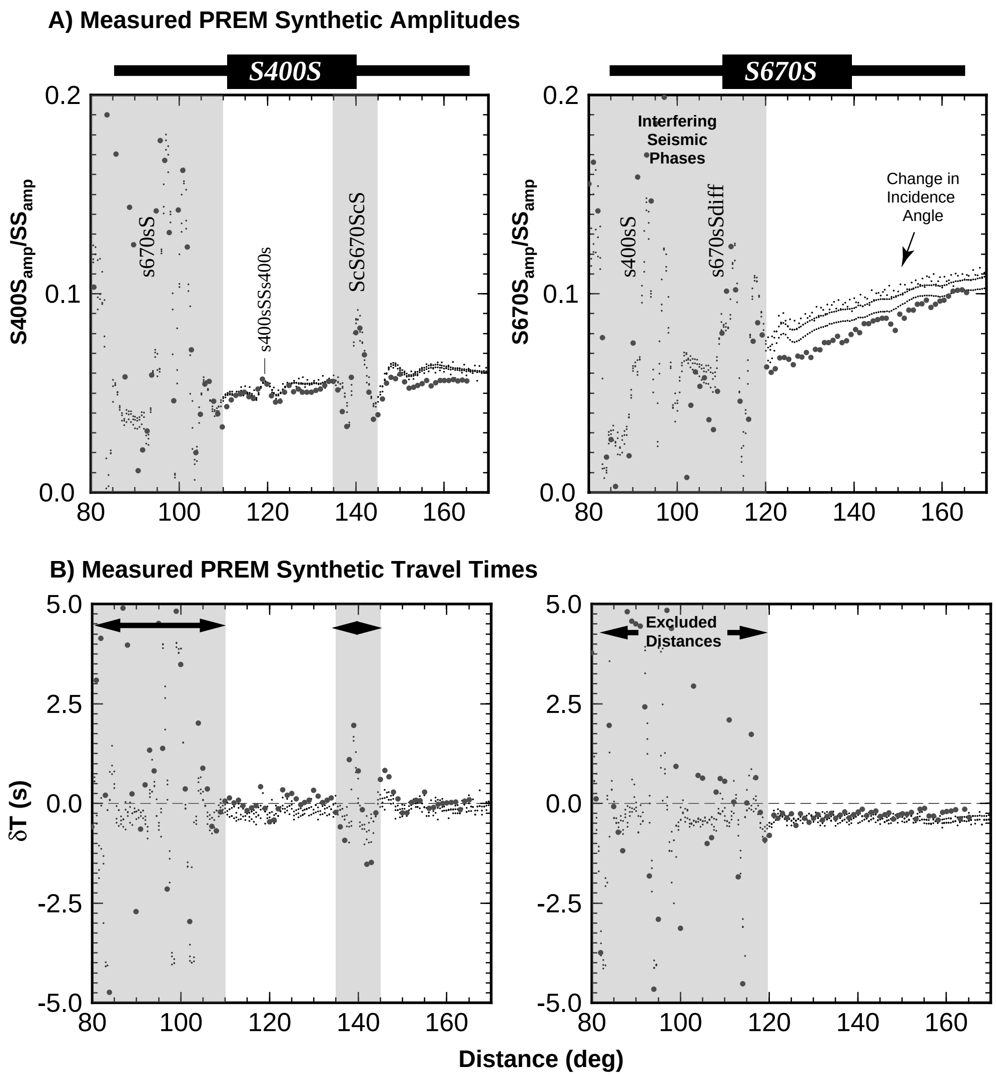

Fig. S2. Synthetic seismogram amplitudes and travel times, and associated errors with interfering phases. The distance windows excluded in our S400S and S670S stacks (Fig. S1) are shaded in light gray. The dominant interfering phase names are shown (again, labeled using PREM discontinuity depths rather than the subsequently determined global average of discontinuity depths of 410- and 660-km (1)). Results are shown for reflectivity synthetics generated every 0.5 degrees in distance from 80-170º, and for event depths of 0, 15, and 30 kilometers. Each measurement on the synthetics is represented by a small black dot. Also shown are the results for the same measurements on the 1º epicentral distance synthetic stacks (large gray dots) as in Fig. S1B. (**A**) The maximum amplitude measured in ±5 second window centered on the PREM predicted arrival time for each precursory phase relative to the amplitude measured at the peak of the SS phase. Amplitude ratios vary sporadically at distances where interfering phases cross the S400S and S670S wave field. The weak upward slope in the S400S/SS ratios with growing distance and more pronounced slope in S670S/SS ratios are due to changing incidence angles (and hence reflection coefficients) of the respective precursor and associated SS phase. (**B**) Differential arrival time perturbation $[(SdS\text{-}SS)_{obs}-(SdS\text{-}SS)_{PREM}]$ (d=400,670-km) of the peak amplitude measured in a ±5 second window around the predicted PREM travel time for each precursor and epicentral distance. Where interfering phases pass through the precursor wave field, as in (**A**), travel time perturbations become large (≥ 3 seconds). Without excluding epicentral distance windows containing such interfering phases (i.e., the shaded regions), these travel time errors propagate into erroneous discontinuity topography estimates, especially for geographic bins biased with data in such distance ranges. Perturbation in the predicted arrival time from varying event depths is less than ±0.5 seconds. The epicentral distance stacks that mirror the distribution of depths and distances in the dataset show that inclusion of deeper events introduces ≤ 0.5 seconds of travel time perturbation.

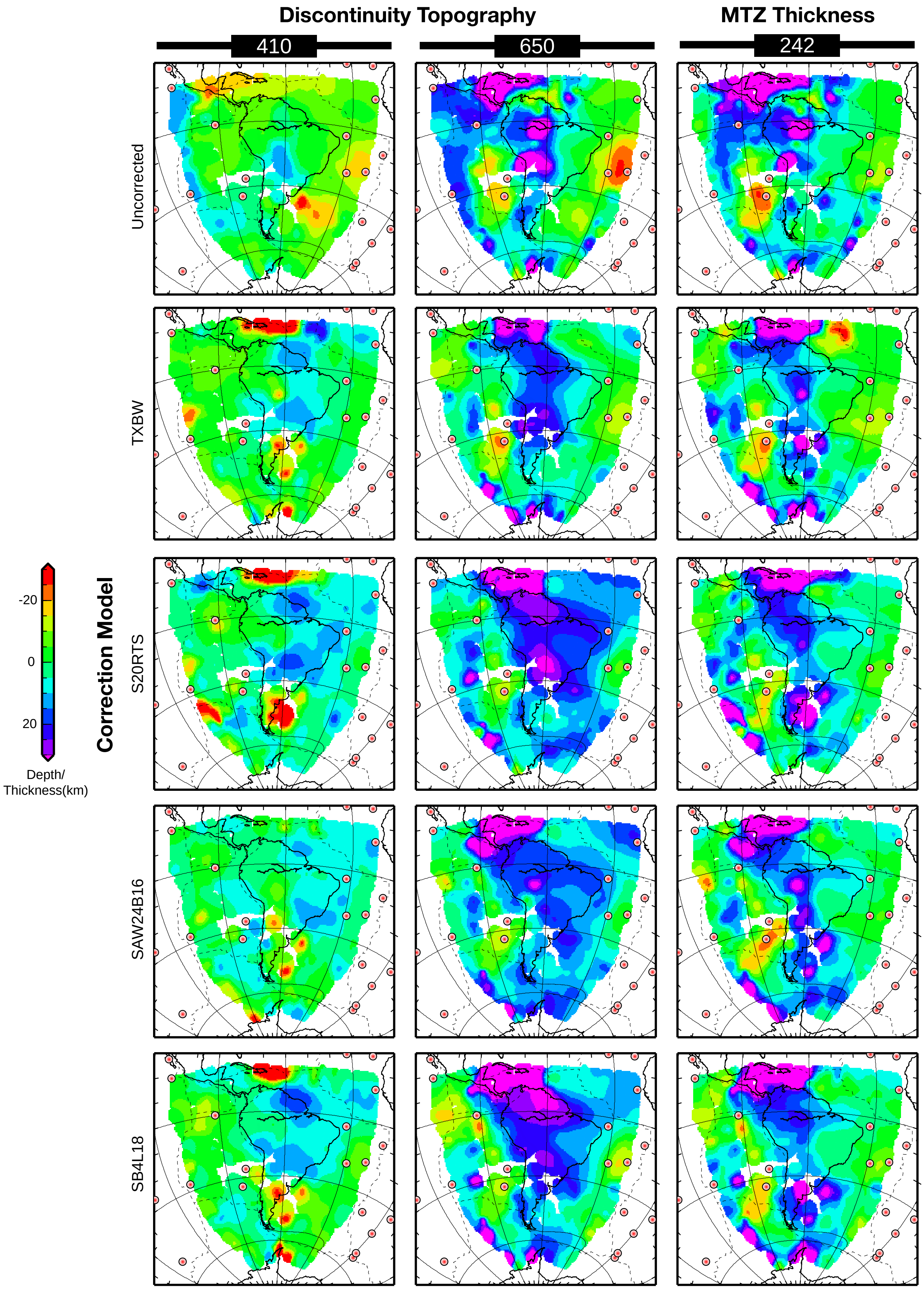
Discontinuity Topography
MTZ Thickness
410
650
242
Uncorrected
TXBW
S20RTS
SAW24B16
SB4L18
Correction Model
-20
0
20
Depth/
Thickness(km)

Fig. S3. 410- and 660-km discontinuity topography and mantle transition zone (MTZ) thickness derived using different tomographic models for correction of heterogeneity along the SS and SS precursor wave paths. The discontinuity topography is shown relative to 410-km and 650-km, the approximate average depths for our study region. Transition zone thickness is shown relative the global average of 242 km (5). Maps are for data low-pass filtered at 10 seconds. Stacks are computed for 1000-km radius bins, as described in the main text. Regions in white correspond to no or sparse data coverage. Significant structural complexity exists for many of the bootstrap-resampled stacks at this frequency (see Fig. 2); thus for these maps we use an average of the depths within each bootstrap histogram to construct these discontinuity topography and mantle transition zone thickness maps. Plate boundaries (dotted lines) (30) and hotspots (red circles) (31) are shown for reference. Maps are shown for the uncorrected results (no upper mantle correction or crustal thickness/topography correction) in the top row, with subsequent rows of panels corresponding to models TXBW (*S10*), S20RTS (*S11*), SAW24B16 (*S12*), and SB4L18 (*S13*). The main difference between the models is a baseline shift in the mean depth of the topography values. Otherwise, lateral variations in features remain similar between the various models, particularly the depression in the 410-km discontinuity to the east of the subducting Nazca slab and the large "troughs" on the 660-km discontinuity in the vicinity of subduction throughout our study region. Similarly, evidence for multiple reflectors associated with the 410- and 660-km discontinuities persists across tomographic models (not shown).

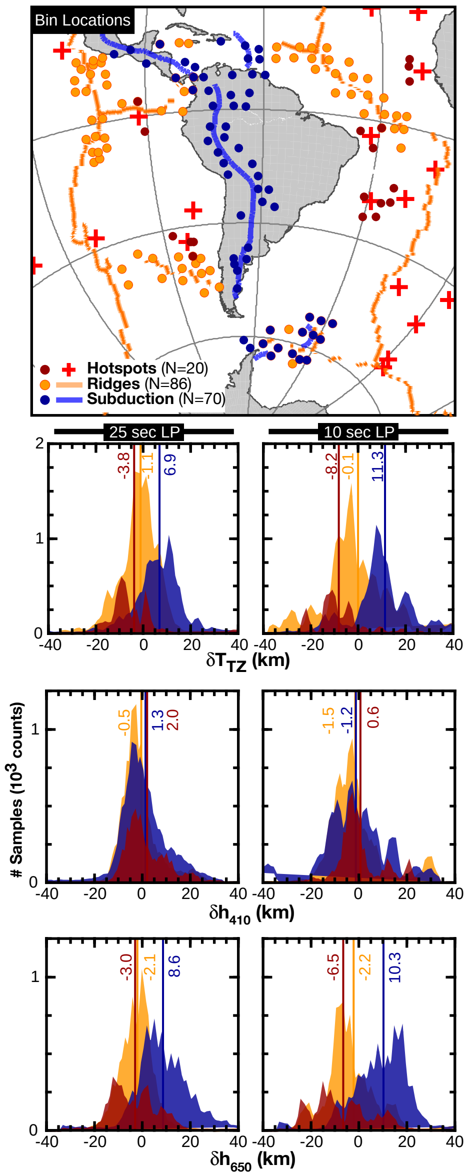

Fig S4. (Top panel) Bin locations compared to tectonic features: bins falling within 500-km of subduction (blue), mid-ocean ridge spreading centers (orange), and/or mantle hotspots (red), are shown. Histograms of mantle transition zone thickness, depth of the 410- and 660-km discontinuities, derived from bootstrap resampling for each bin, are displayed relative to a mean of 242-km, 410-km, and 650-km, respectively, for the short

(10 seconds) and long (25 seconds) period data. Bins near subduction were selected by projecting the subducting slab to 530-km depth using tomographic images and the location of deep seismicity (*S14*). Hotspots are from the catalog of (31). The vertical lines in the lower panels demark mean histogram values for each feature. Transition zone thickness correlates with the expected thermal structure for each tectonic province, though there is more complexity in distributions derived from shorter period data (see Fig. S3 and supplemental text).

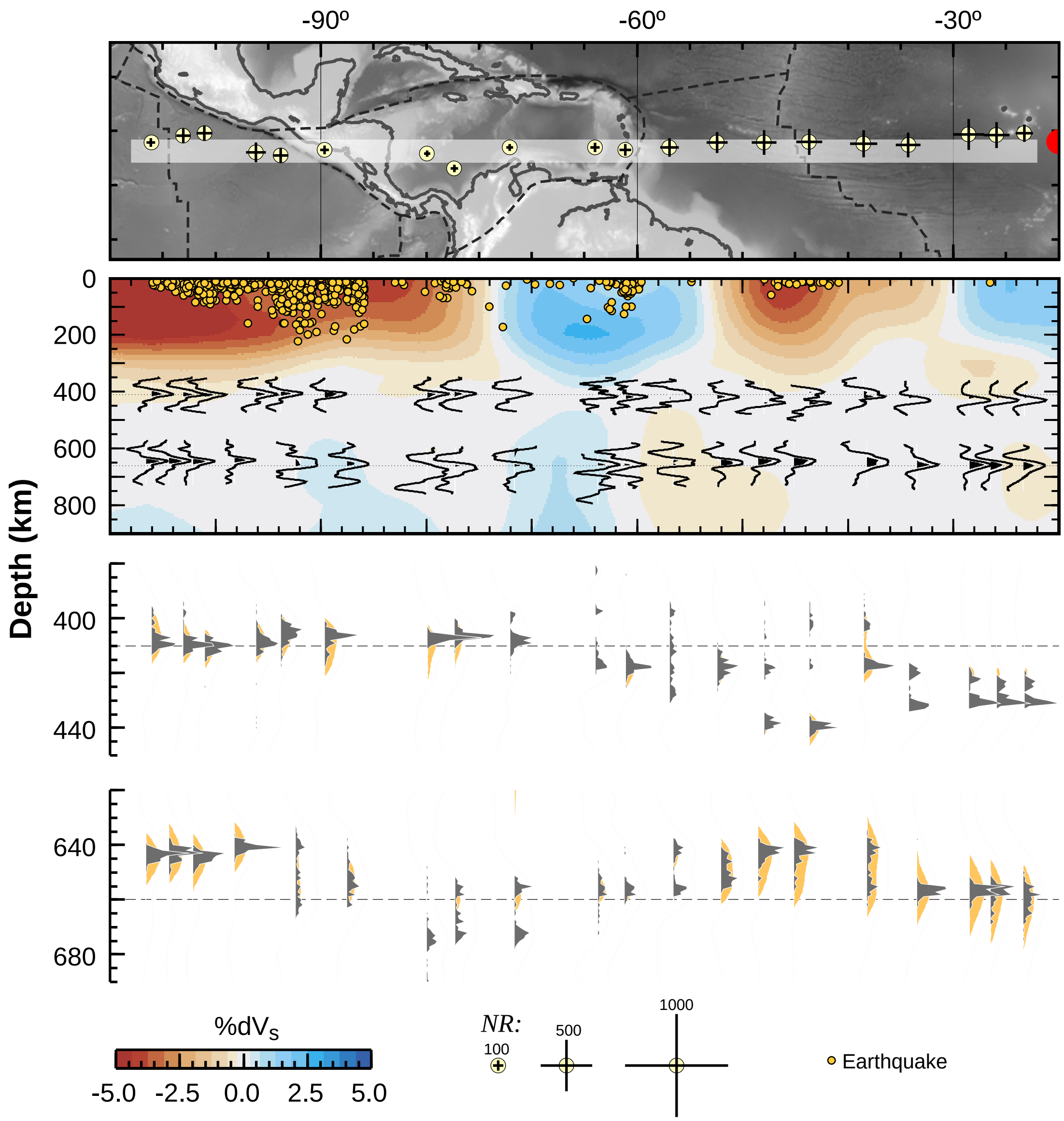

Fig. S5. Cross-section of discontinuity structure at 13ºN latitude; with the addition of a tomography cross-section through the TXBW model (*S10*). The top panel shows the cross-section location, average stack locations, and number of records in each stack (scale given on bottom), as well as earthquakes from (*S14*) falling beneath 300-km depth (orange circles), hotspots (red circles), and the plate boundaries (30) (black dotted line).

In the tomography cross-section, relative velocities are given in the scale at the bottom of the plot, as well as earthquakes falling within 5º of the cross-section location (orange circles), stacked energy (solid black lines), and energy falling above the 95% confidence interval (solid black shading). Below the tomography cross-section, the topography on the 410- and 660-km discontinuities is shown (as in Fig. 3). In all subsequent cross-sections (Figs. S6-S15), the horizontal scale is adjusted to be relative to this figure, removing any horizontal distortion between the panels.

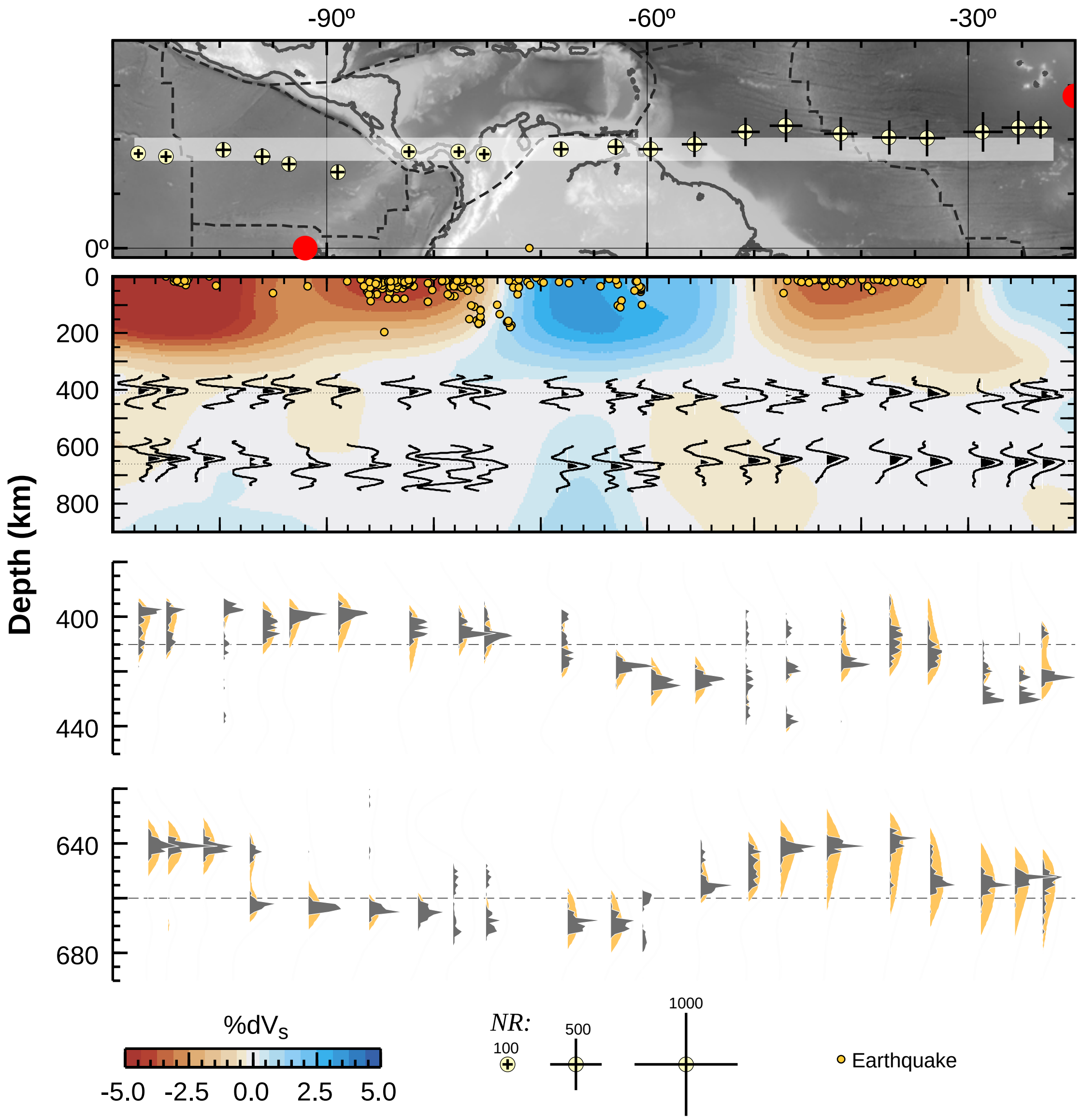

Fig. S6. Cross-section of discontinuity structure at 8ºN latitude. All details are as in (Fig. S5). This cross-section corresponds to cross-section A-A' in (Fig. 3).

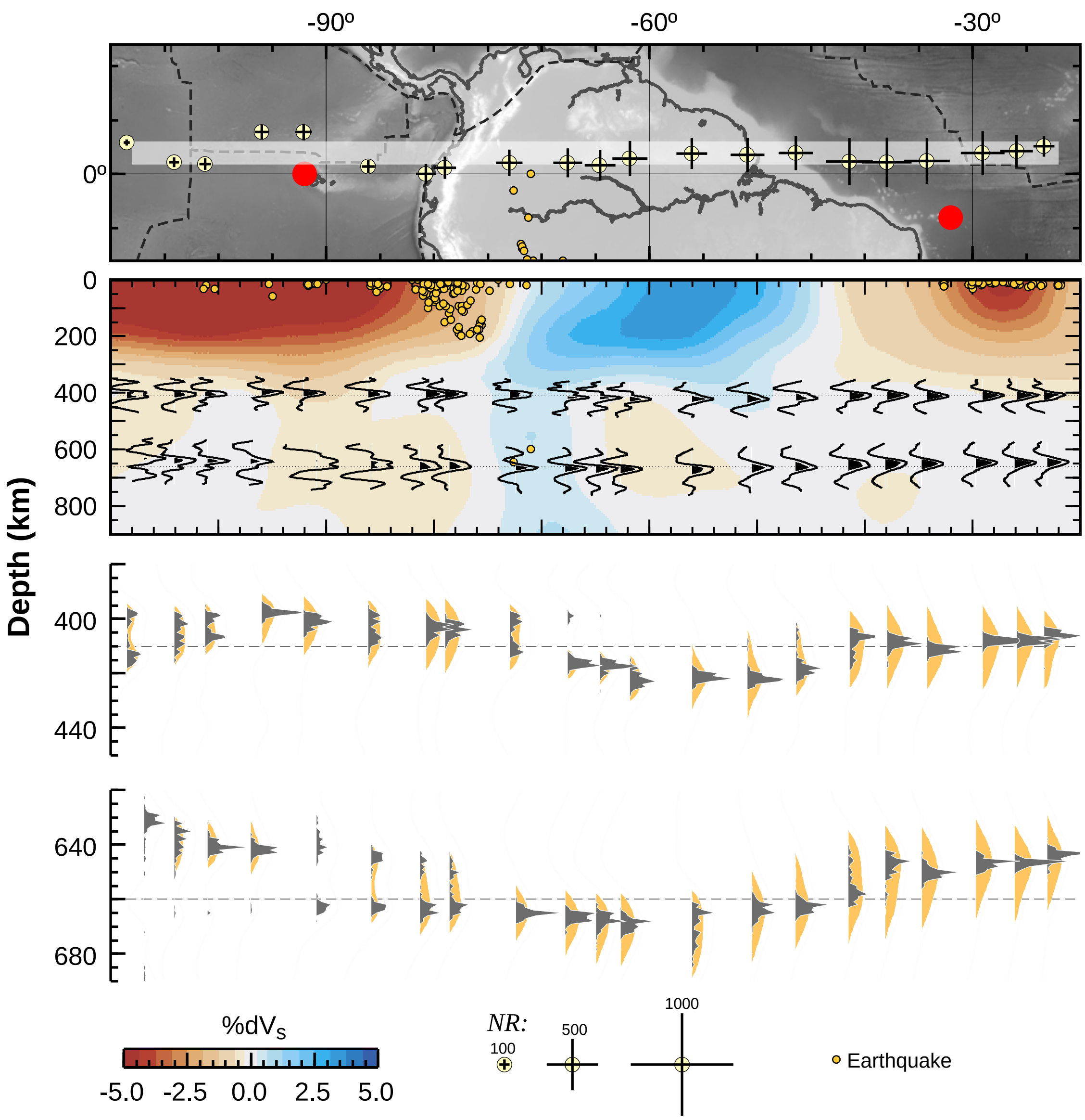

Fig. S7. Cross-section of discontinuity structure at 3ºN latitude. All details are as in (Fig. S5). This cross-section corresponds to cross-section B-B' in (Fig. 3).

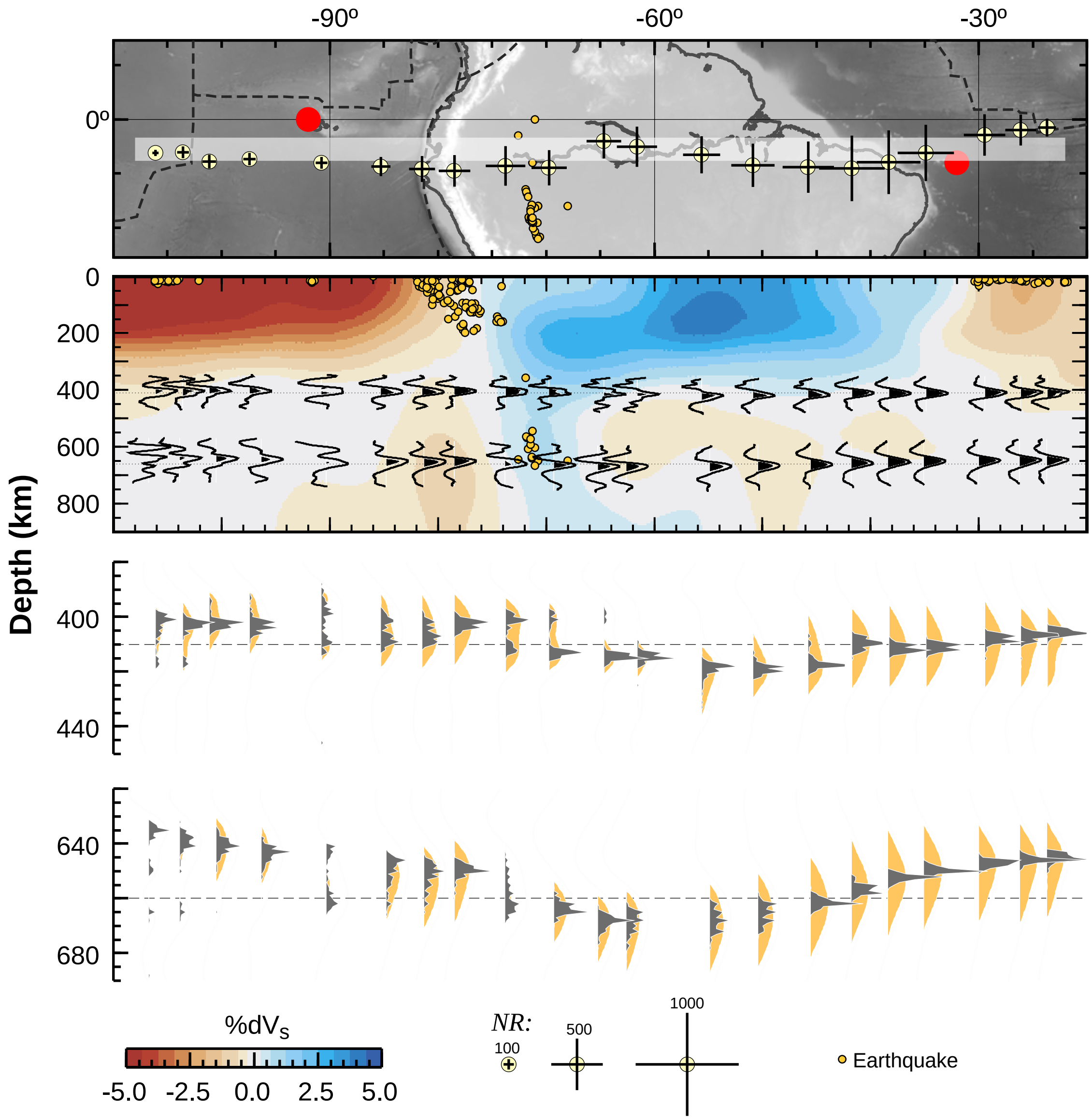

Fig. S8. Cross-section of discontinuity structure at 3ºS latitude. All details are as in (Fig. S5). This cross-section corresponds to cross-section C-C' in (Fig. 3).

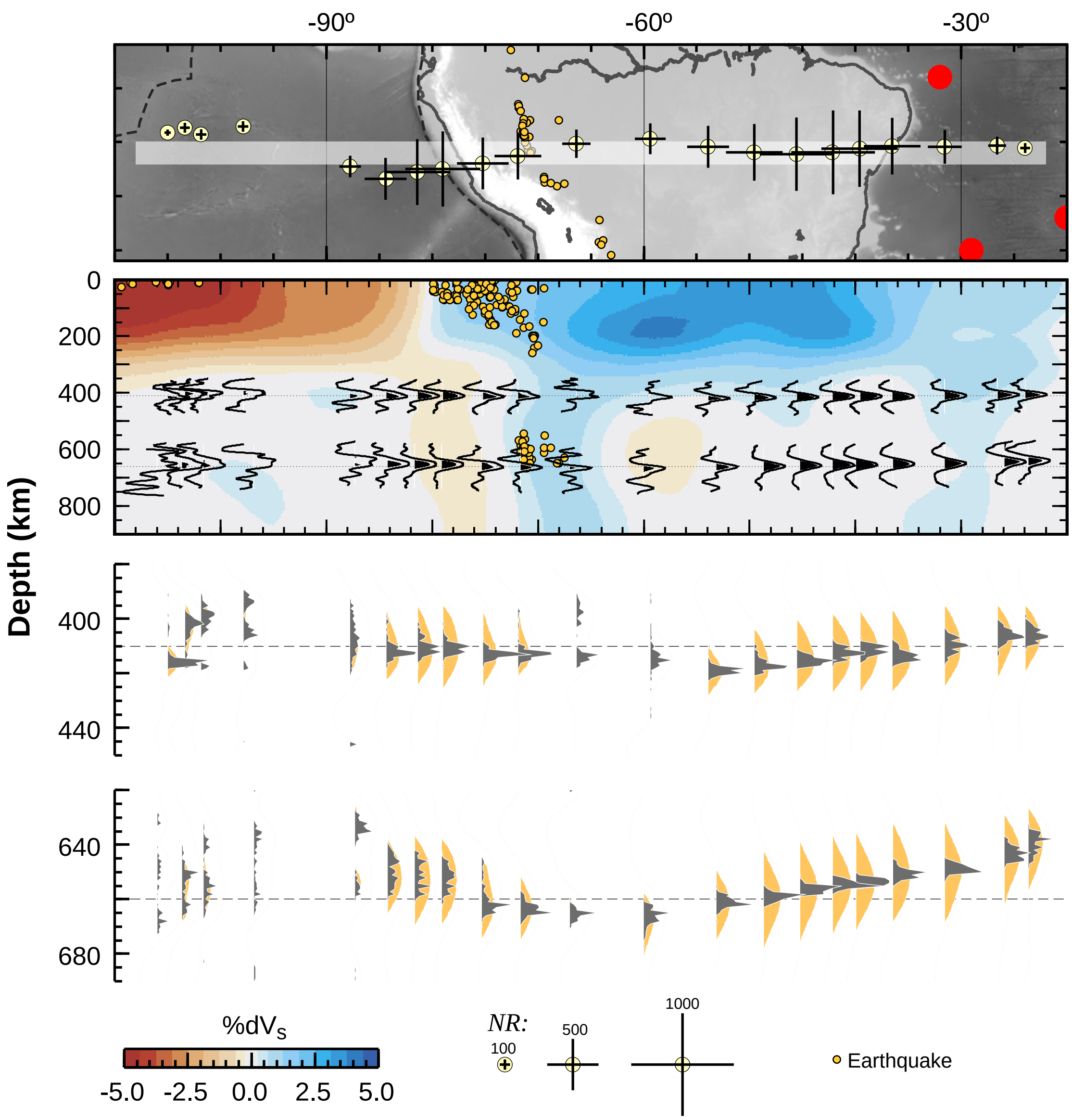

Fig. S9. Cross-section of discontinuity structure at 12ºS latitude. All details are as in (Fig. S5). This cross-section corresponds to cross-section D-D' in (Fig. 3).

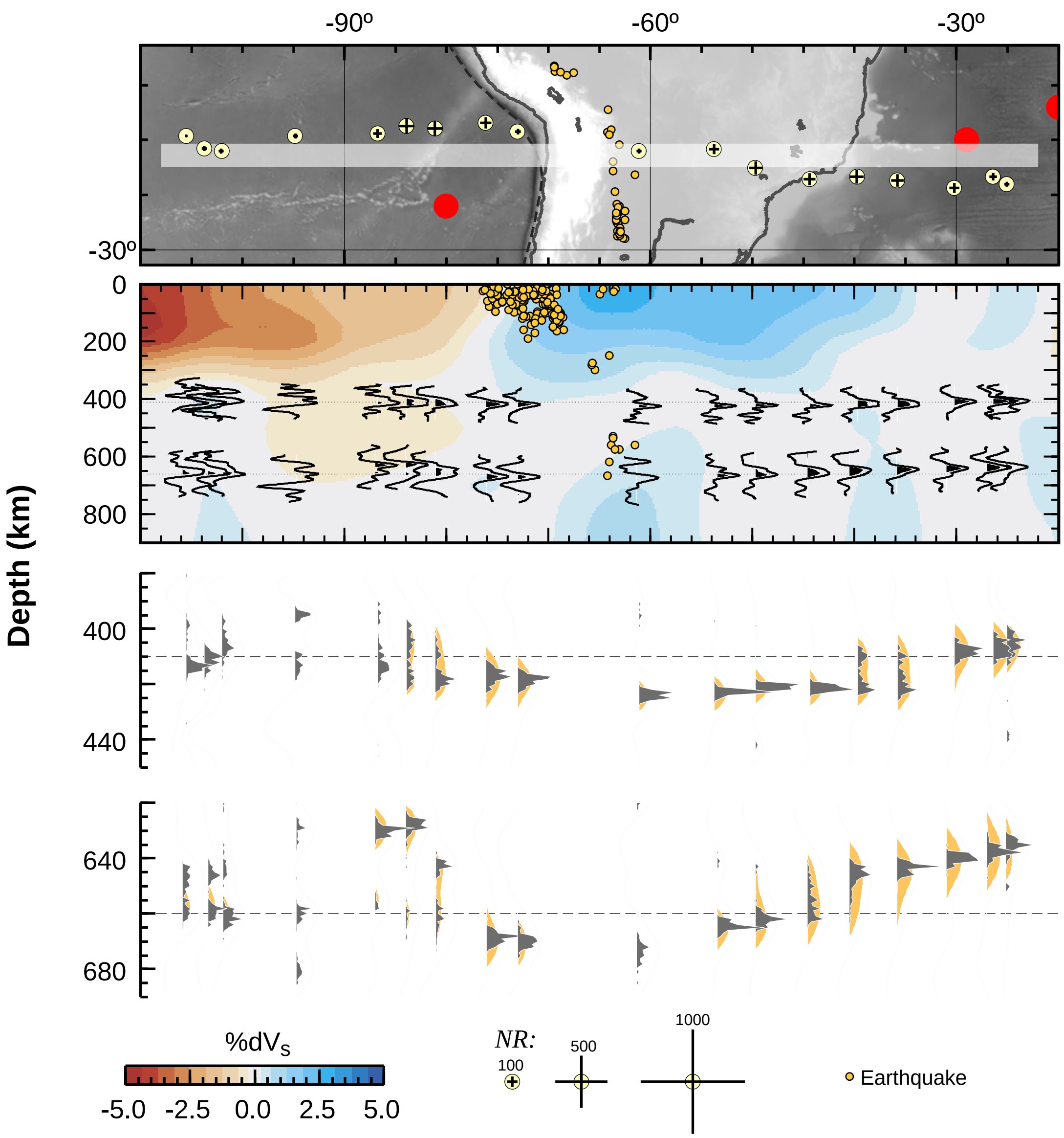

Fig. S10. Cross-section of discontinuity structure at 22ºS latitude. All details are as in (Fig. S5). This cross-section corresponds to cross-section E-E' in (Fig. 3).

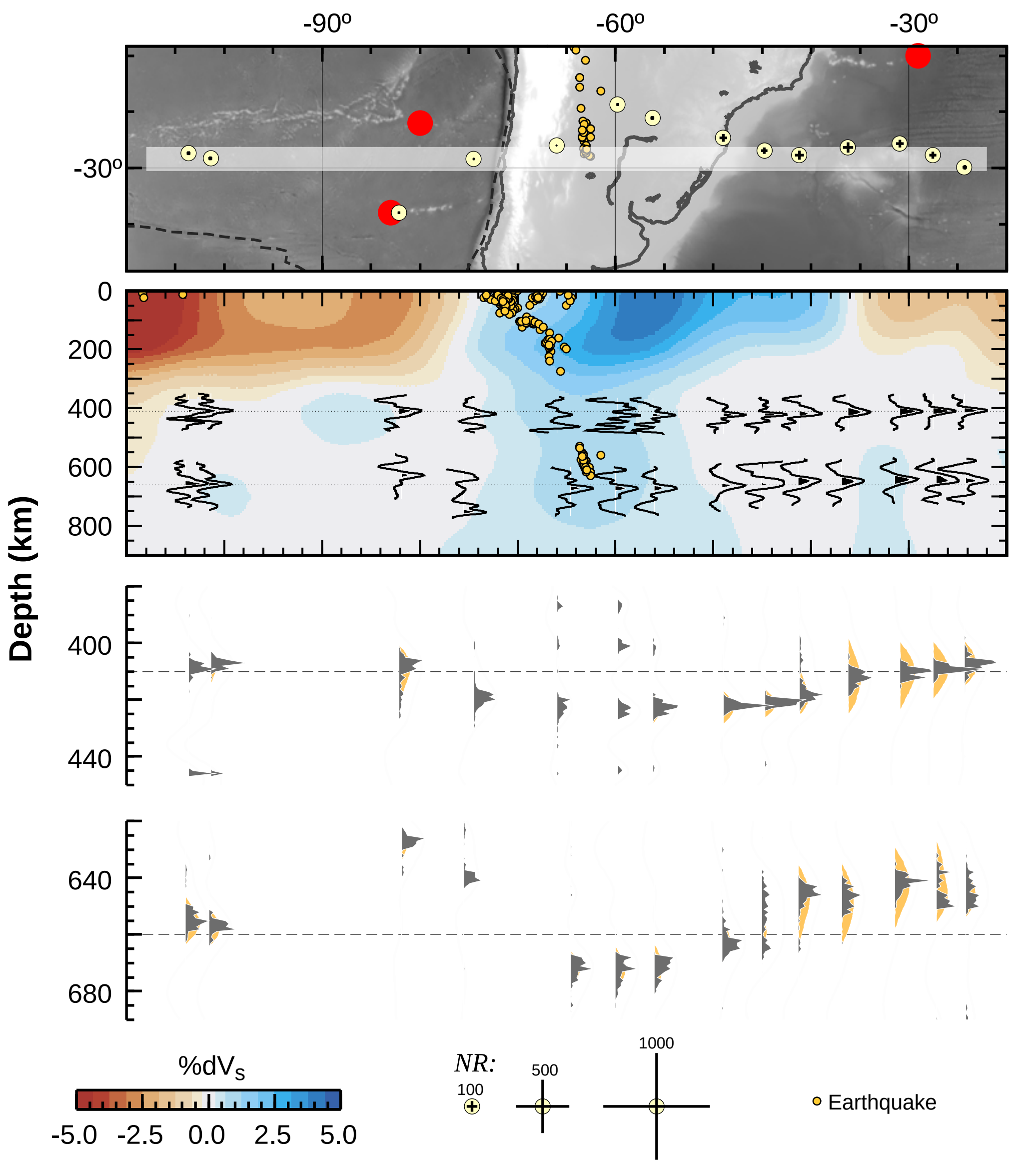

Fig. S11. Cross-section of discontinuity structure at 28ºS latitude. All details are as in (Fig. S5).

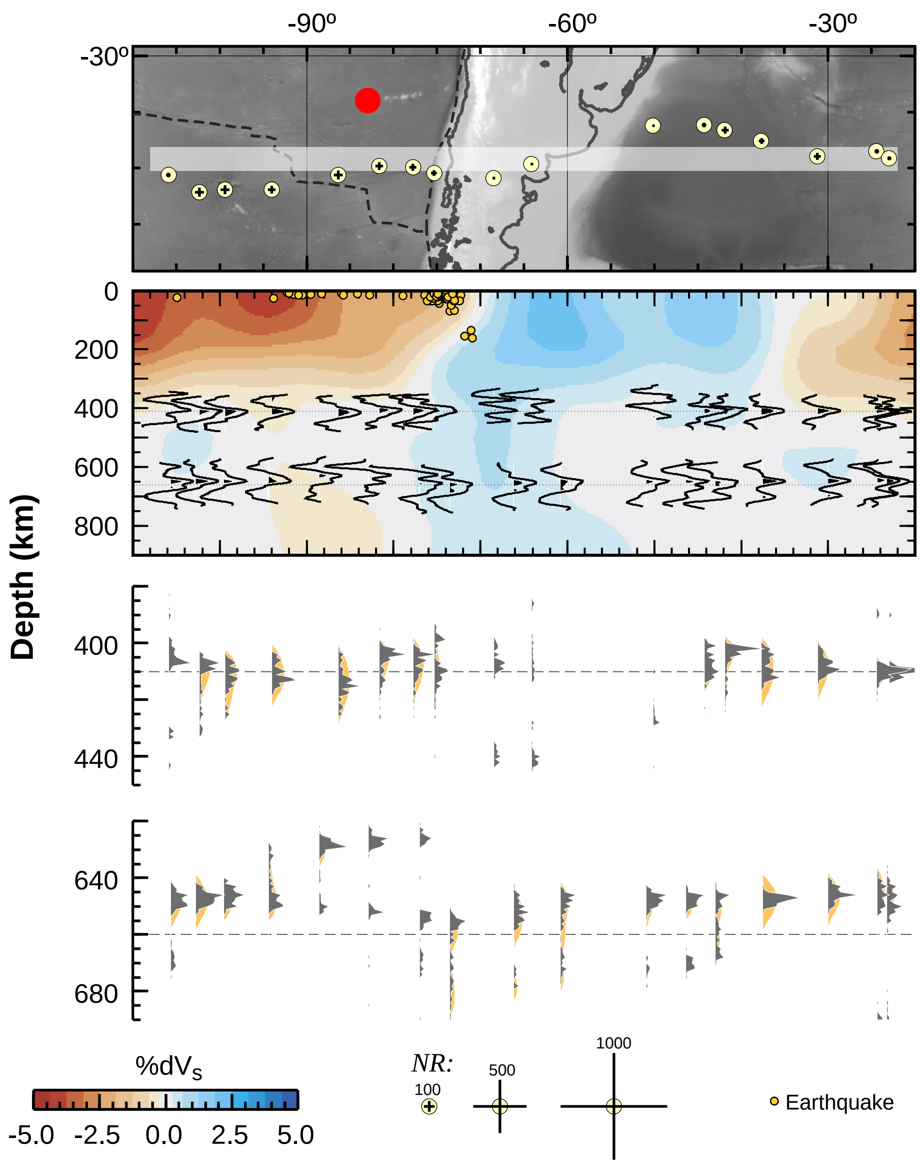

Fig. S12. Cross-section of discontinuity structure at 39ºS latitude. All details are as in (Fig. S5).

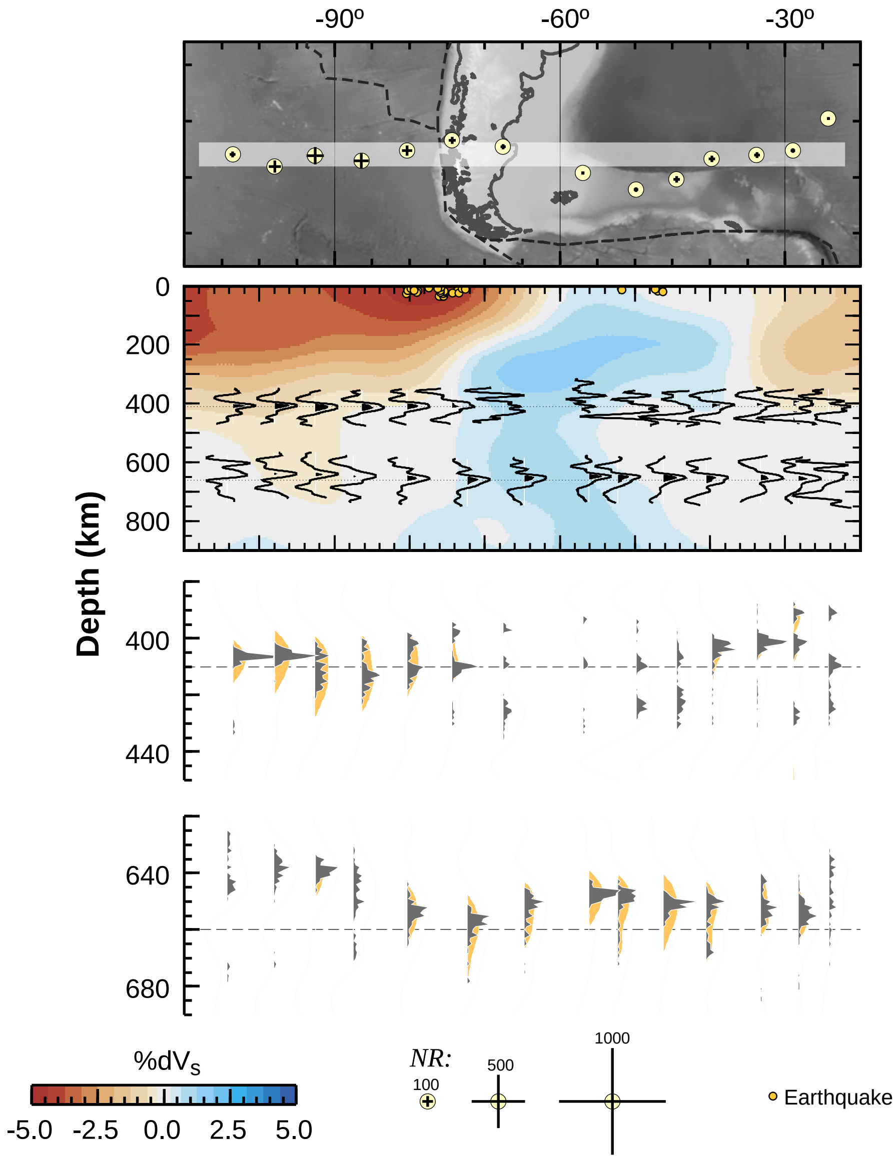

Fig. S13. Cross-section of discontinuity structure at 48ºS latitude. All details are as in (Fig. S5).

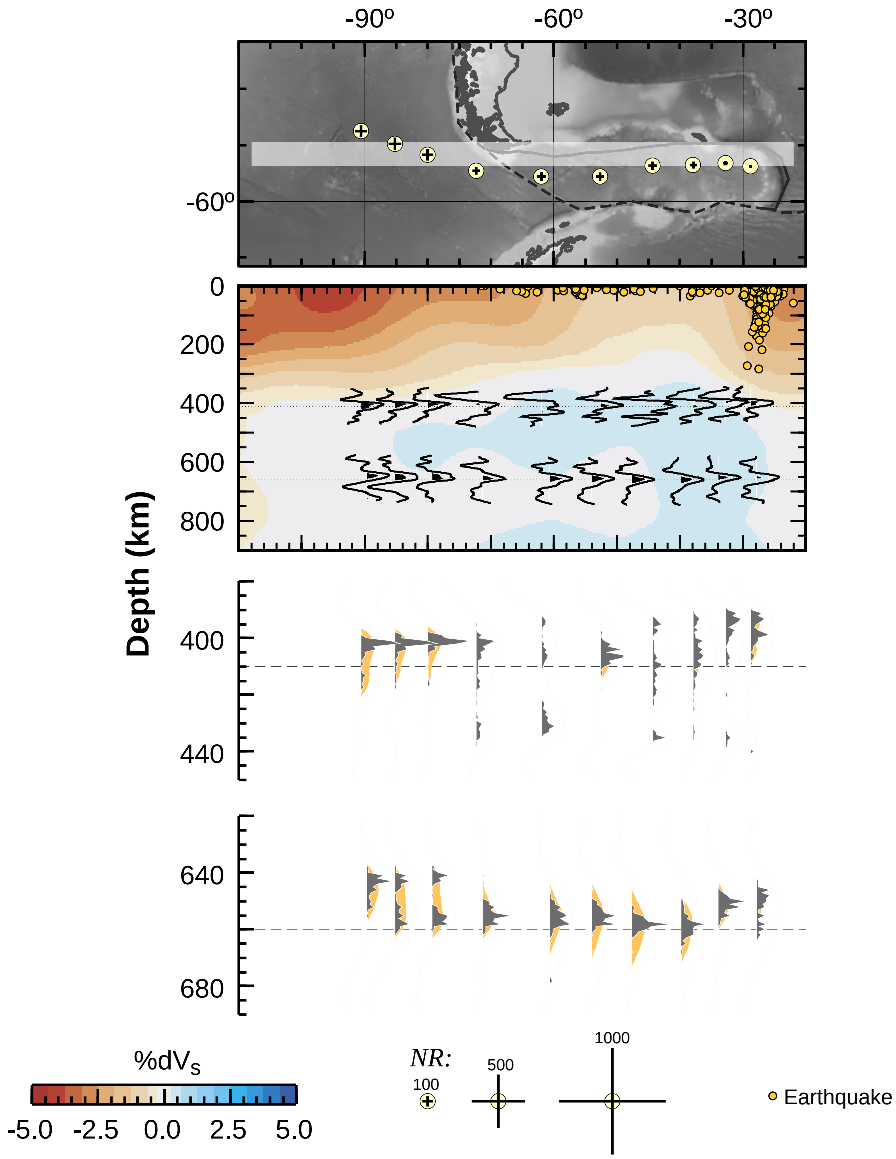

Fig. S14. Cross-section of discontinuity structure at 56ºS latitude. All details are as in (Fig. S5).

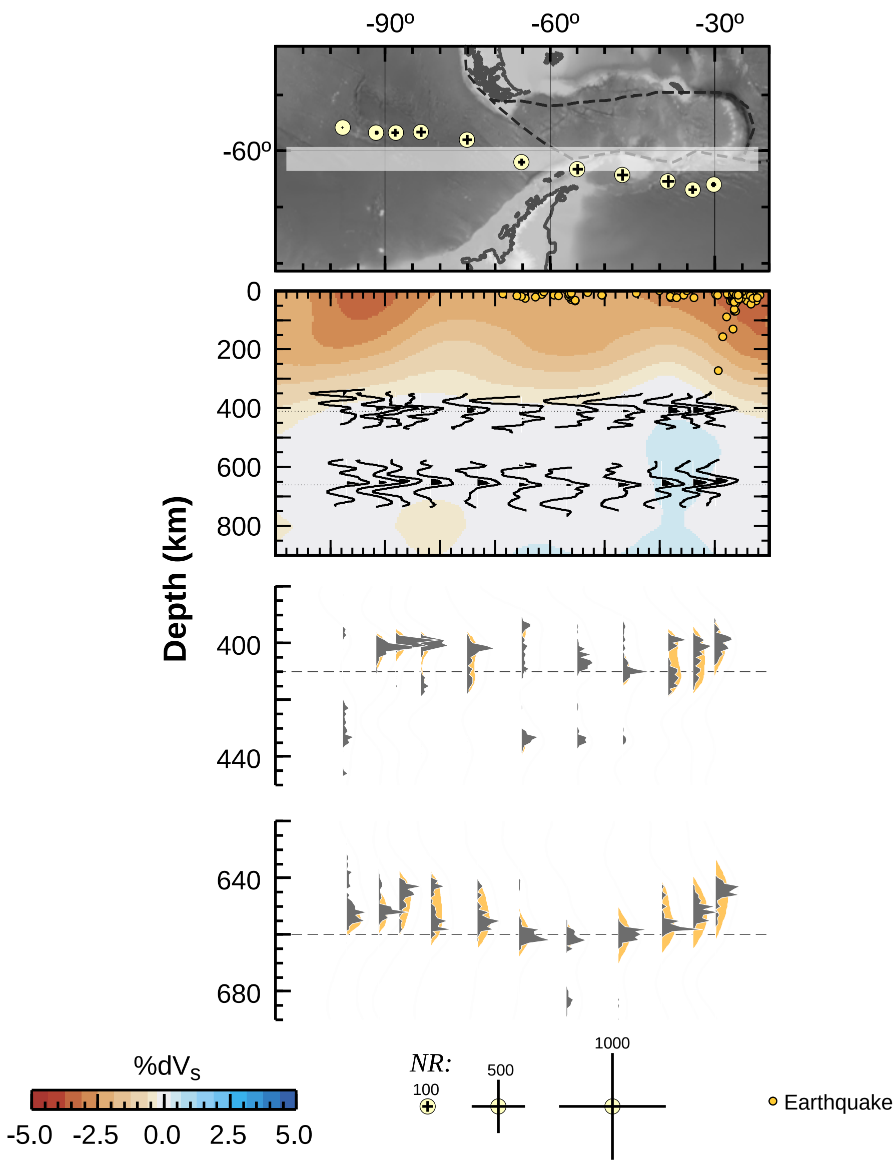

Fig. S15. Cross-section of discontinuity structure at 61ºS latitude. All details are as in (Fig. S5).

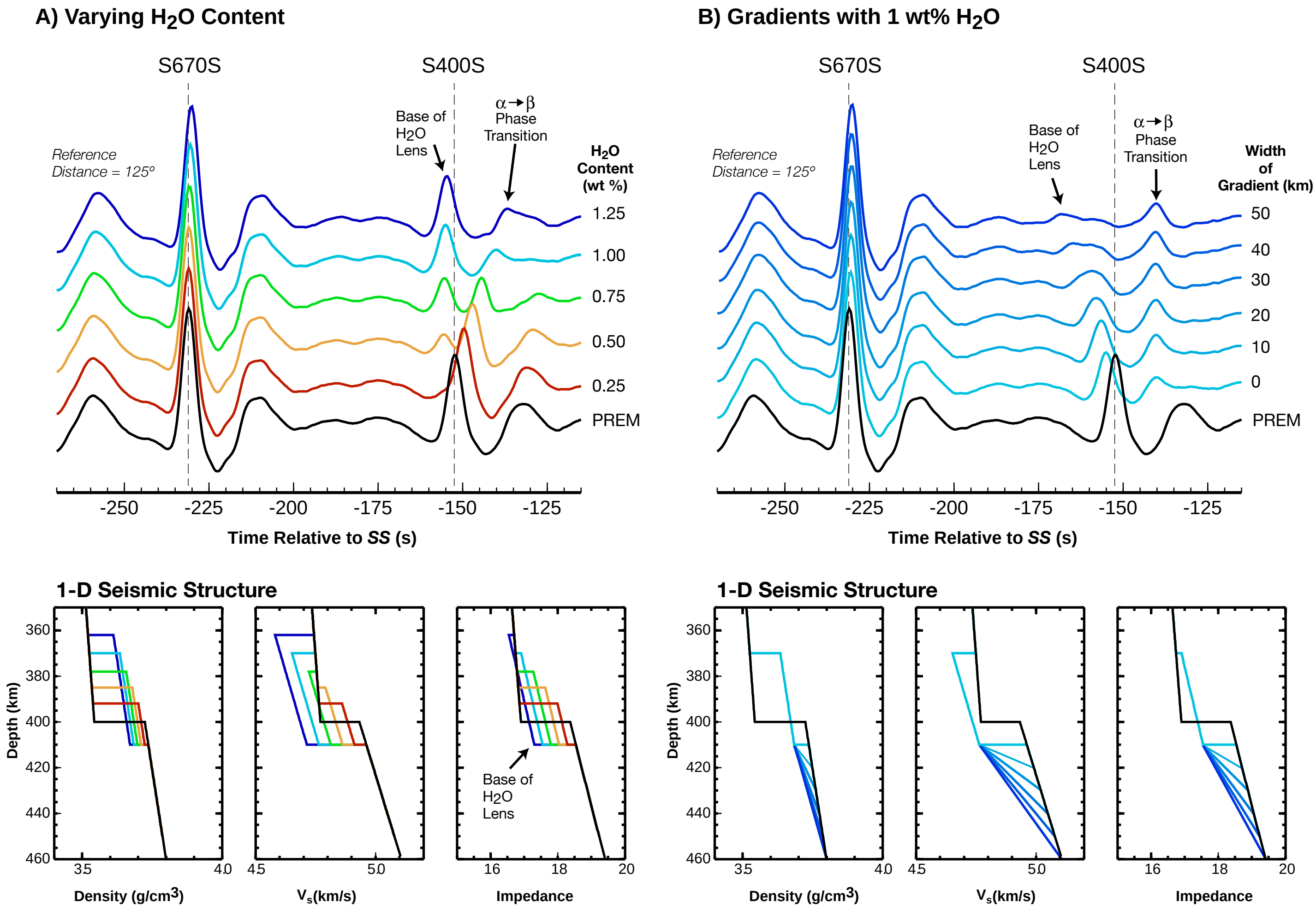

Fig. S16. Reflectivity synthetic seismograms showing S670S and S400S for varying amounts of H_2O content in the transition zone mineral wadsleyite. A perturbation of the depth of the 400-km discontinuity in the model is calculated using

$$\Delta Z = \left(\frac{\delta Z}{\delta C_{H_2O}}\right) \cdot C_{H_2O} \quad \text{(Eq. 1)}$$

where ΔZ is the change in depth (km) of the 400-km discontinuity (note that we use the PREM value here, not the global average), C_{H2O} is the H_2O content (in weight %), and $\delta Z/\delta C_{H2O}$ is the discontinuity depth dependence on H_2O content (km/(wt% H_2O)), given a value of –30 as in (22). The velocity reduction in the hydrated wadsleyite, δv_s^{H2O} (km/sec), is found using

$$\delta v_s^{H_2O} = v_s - A \cdot C_{H_2O} \qquad \text{(Eq. 2)}$$

where v_s is the unhydrated shear wave velocity, C_{H2O} is the H_2O content of the anomaly (in weight %), and A is a constant (km/[sec*wt% H_2O]), given a value of 0.04 computed from (22), which is similar to the 0.036 value cited in (*S15*) for ringwoodite. To obtain a density reduction in the hydrated lens, $\delta\rho^{H2O}$ (g/cm^3), v_s in Eq. 2 can be replaced by density ρ; we use *A*= 0.014, computed from a 1.4% reduction in density for 1 wt% H_2O in ringwoodite (*S15*). Based upon the similarity of the A values for δv_s^{H2O}, the A value for $\delta\rho^{H2O}$ in wadsleyite is likely comparable to that in ringwoodite. This does not account for other mantle phases and the effect of hydration on their properties; the model also assumes wadsleyite is the dominant mineral controlling seismic wave speeds and density. Thermal effects would shallow the 410-km discontinuity in the vicinity of subduction (further enhancing the effect of hydrogen), so we do not include those here. (**A**) Reflectivity synthetic waveforms for increasing H_2O content in our models. The seismic structure for each model is given below the waveforms. We use seismograms at a distance of 125º, as there are few interfering phases with S670S and S400S, simplifying interpretation of waveforms. Predicted PREM arrival times for each precursor (gray dotted lines) are shown in the waveform plot. The phase transition of olivine to wadsleyite (labeled $\alpha\rightarrow\beta$ in the figure) is shallower with increasing H_2O content, and the impedance contrast drops as a result of shear wave and density reduction in the hydrated wadsleyite. The base of the hydrated lens is fixed at 410-km depth (see lower panels), and the depth of the $\alpha\rightarrow\beta$ phase transition is computed using (Eq. 1); increasing levels of hydration within the lens create a stronger impedance contrast at its base. (**B**) We explore a number of gradients, where hydration in the lens starts at 1 wt% H_2O and decreases linearly over the depths below the 410-km boundary rather than ending abruptly the base of the lens. A gradient is expected rather than a sharp boundary from the diffusion of hydrogen in the mantle. The width of such a gradient is dependent upon the diffusion rate of H_2O in the mantle, recent experiments by (*S16*) find it to be relatively slow: on the order of 5.3 km in 10^9 years at 1450ºC. Regardless, we still explore several gradient models and find a weak reflection of energy is still detectable at both the olivine-to-wadsleyite phase transition and near the base of the lens for gradients up to 50 km in width. This modeling suggests that H_2O concentration ≥ 0.75 wt% in the lens and basal gradients of < 50 km can provide sufficient reflection of seismic energy to image a hydrated wadsleyite lens, matching our observations.

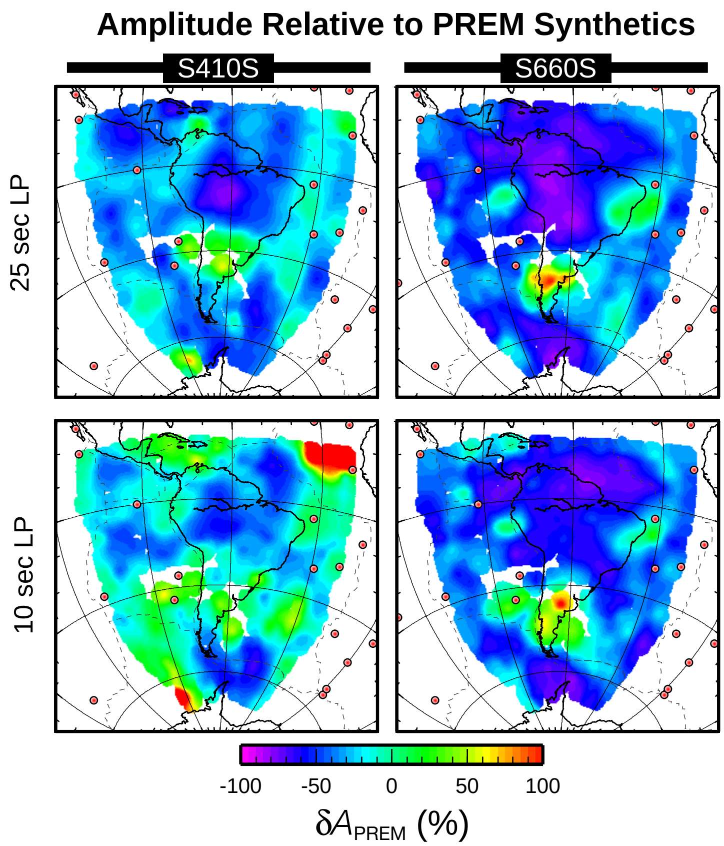

Fig. S17. Amplitudes of the stacked S410S and S660S precursors referenced to SS, relative to the amplitude ratios predicted by stacking PREM synthetics. The synthetic stacks are generated using the same source depths and distance distribution as in the data, thereby making a prediction for the amplitude in each stack. The amplitude ratio is computed using:

$$\frac{SdS/SS_{data} - SdS/SS_{PREM}}{SdS/SS_{PREM}} \times 100 = \delta A(\%) \qquad \text{(Eq. 3)}$$

Where SdS is the precursor depth (d=410,660-km), SS_{data} is the measured amplitude of the SS phase in the data stack, SS_{PREM} is the predicted amplitude of the SS phase from the synthetic stack of PREM seismograms, and ∀A is given in percent. The maximum amplitude for each precursor is measured in a ±15 second window around the expected

PREM arrival time. The top row shows the results for the 25-second low pass data, and the second row the result for the 10-second low pass filter. Hotspots (red dots) and plate boundaries (dotted black lines) are the same as in Fig. S3. Past work suggests (*S17*) the 410-km discontinuity reflection coefficient values should be similar to PREM, and that the 660-km value is likely 50% of the PREM value. For both dominant periods, our 660-km amplitudes roughly agree with this result, and are 50% or less of the PREM value (blue color). However, the pattern of reflected energy amplitude on the 410-km discontinuity is frequency dependent, though in most regions it is within ±20% of the PREM value. The 410-km discontinuity becomes weaker underneath the northern part of the South American continent and the Scotia microplate. The weakest S410S precursor amplitudes are associated with the region showing a depressed 410-km boundary, which is where we infer the lens of elevated H_2O content just below this interface. For both discontinuities, the weakest reflectors are generally associated with subduction, though there is some complexity at shorter periods from the appearance of multiple discontinuities. It is also important to consider that precursor amplitudes are closely tied not just to discontinuity sharpness, but also to topographic relief (*S18*, *19*). Waveform scattering and mantle heterogeneity may defocus precursory amplitudes, both of which are generally expected in the vicinity of subduction. Both of these effects are consistent with reduced amplitudes in the presence of large-scale relief and compositional heterogeneity.

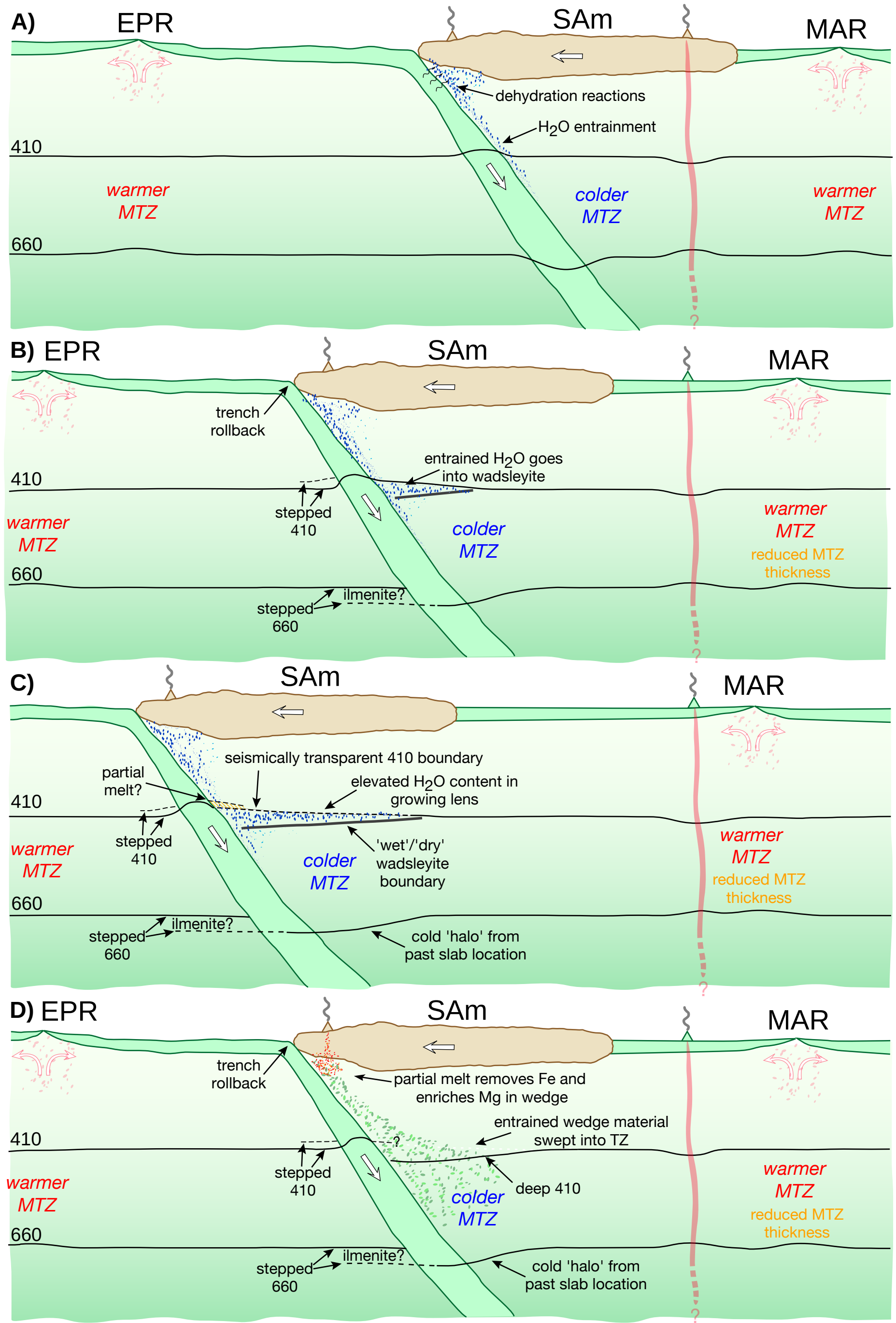

Fig. S18. Time progression of the formation of a H_2O-rich lens under-plating the 410-km discontinuity in cross-section view (Fig. 4). Continued trench migration contributes to the evolution of a lens of wadsleyite with an elevated H_2O content, the base of which is detected in our study. (**A**) H_2O is brought into the transition zone either by entrainment of hydrated upper mantle materials and/or transported within the slab. As the South American continent moves westward due to trench rollback (**B**), the buoyant hydrated wadsleyite collects at the top of the transition zone, elevating the 410-km discontinuity as the hydrated lens forms. (**C**) Final lens geometry (Fig. 4). (**D**) A depressed 410-km boundary due to Fe depletion in the olivine system. Fe-depleted regions are shown as stippled green dots. Melting (red dots) in the wedge increases the Mg content of the $(Mg,Fe)_2SiO_4$ residue from the expected Mg_{89} to $Mg_{92\text{-}94}$ (*S20*). These magnesium-enriched wedge materials are entrained by viscous coupling of the slab with the overlying mantle, and transported into the MTZ. A 3-4% increase in the Mg content of the olivine results in an increased the depth of the 410-km discontinuity by 7-10 km, based upon the compositional Clapeyron slopes shown in (24). In this model, multiple discontinuities observed at 410-km depth, could be explained by localized thermally induced up-warping of the 410-km within the cold subducting slab lying next to a deep 410-km boundary in the Mg-rich mantle. The presence of a metastable wedge of olivine within the slab would produce complex topography on the 410-km boundary, and may also be responsible for the observation of multiple discontinuities. Hydrous melting at the 410-km discontinuity may enhance the Fe-depletion; this would further increase the effective content of Mg in the subducted materials entering the MTZ.

References and Notes:

S1. http://www.iris.edu
S2. http://earthquakescanada.nrcan.gc.ca
S3. http://www.earthscope.org/
S4. A. M. Dziewonski, D. L. Anderson, *Phys. Earth. Planet. Inter.* **25**, 297 (1981).
S5. C. Bassin, G. Laske, M. G., in *Eos*. (Fall Meeting Suppl., San Francisco, CA, 2000), vol. 81, pp. F897.
S6. http://www.ngdc.noaa.gov/
S7. L. Zhao, S. Chevrot, *Geophys. Res. Lett.* **30**, 1590 (2003).
S8. P. M. Shearer, *J. Geophys. Res.* **101**, 3053 (1996).
S9. G. Müller, *Journal of Geophysics* **58**, 153 (1985).
S10. S. P. Grand, *Philos. Trans. R. Soc. London, Ser. A* **360**, 2475 (2002).
S11. J. Ritsema, H. J. van Heijst, J. H. Woodhouse, *Science* **286**, 1925 (1999).
S12. X. D. Li, B. Romanowicz, *J. Geophys. Res.* **101**, 22245 (1996).
S13. G. Masters, G. Laske, H. Bolton, A. M. Dziewonski, in *Earth's Deep Interior: Mineral Physics and Tomography From the Atomic to the Global Scale*, S. Karato, A. Forte, R. Liebermann, G. Masters, L. Stixrude, Eds. (AGU, Washington D.C., 2000), vol. 117, pp. 63-87.
S14. E. R. Engdahl, R. van der Hilst, R. Buland, *Bulletin of the Seismological Society of America* **88**, 722 (1998).
S15. S. D. Jacobsen, J. R. Smyth, H. Spetzler, C. M. Holl, D. J. Frost, *Phys. Earth. Planet. Inter.* **143-44**, 47 (2004).
S16. R. Hae, E. Ohtani, T. Kubo, T. Koyama, H. Utada, *Earth. Planet. Sci. Lett.* **243**, 141 (2006).
S17. P. M. Shearer, M. P. Flanagan, *Science* **285**, 1545 (1999).
S18. E. Chaljub, A. Tarantola, *Geophys. Res. Lett.* **24**, 2613 (1997).
S19. F. Neele, H. deRegt, J. VanDecar, *Geophys. J. Int.* **129**, 194 (1997).
S20. Y. Tatsumi, S. Eggins, *Subduction Zone Magmatism*. (Blackwell Science, Cambridge, MA, 1995), pp. 211.